

THESIS FOR THE DEGREE OF LICENTIATE OF ENGINEERING

Studies of the S-type AGB star W Aquilae:

The circumstellar envelope and the faint companion

TAÏSSA DANILOVICH



CHALMERS

Department of Earth and Space Sciences
CHALMERS UNIVERSITY OF TECHNOLOGY
Göteborg, Sweden 2014

**Studies of the S-type AGB star W Aquilae:
The circumstellar envelope and the faint companion**

Taïssa Danilovich

© Taïssa Danilovich, 2013

Radio Astronomy & Astrophysics Group
Department of Earth and Space Sciences
Chalmers University of Technology
SE-412 96 Göteborg, Sweden
Phone: +46 (0)31-772 1000

Contact information:

Taïssa Danilovich
Onsala Space Observatory
Chalmers University of Technology
SE-439 92 Onsala, Sweden

Phone: +46 (0)31-772 5544
Fax: +46 (0)31-772 5590
Email: taïssa@chalmers.se

Cover image:

Molecules in a circumstellar envelope. Not to scale.

Printed by Chalmers Reproservice
Chalmers University of Technology
Göteborg, Sweden 2014

Studies of the S-type AGB star W Aquilae: The circumstellar envelope and the faint companion

TAÏSSA DANILOVICH

Department of Earth and Space Sciences
Chalmers University of Technology

Abstract

Low- and intermediate-mass stars will all eventually enter the asymptotic giant branch (AGB) phase. AGB stars experience intense mass-loss, generating a significant fraction of the dust and atomic and molecular matter that enriches the interstellar medium. AGB stars are also responsible for the production of about half of all elements heavier than iron.

AGB stars can be classified into two broad categories: oxygen-rich M stars and carbon-rich C stars. When a star leaves the main sequence and ascends the AGB, it will initially be oxygen-rich (that is, its surface abundance of oxygen is higher than that of carbon). Over time, for a particular subset of AGB stars, enough carbon will be dredged up from their interiors and, eventually, turn them into carbon-rich stars. S-type AGB stars are believed to be an intermediate evolutionary stage between M and C stars, with a C/O abundance ratio close to 1. As transition objects they provide a unique window into the mass-loss mechanism(s) and chemistry of AGB stars.

W Aql is an S-type AGB star with a binary companion. In this thesis we examine its mass-loss properties through a detailed analysis of the molecular emission in its circumstellar envelope (CSE). With new Herschel/HIFI observations which probe areas of the CSE closer to the star, we are able to better constrain mass-loss and other CSE properties than previously possible. We detect molecular emission lines of CO, H₂O, SiO, HCN and NH₃, the latter for the first time in an S star. We find a mass-loss rate for W Aql of $3.5 \times 10^{-6} M_{\odot} \text{ yr}^{-1}$ and present abundances of each molecular species.

We also use optical observations of the W Aql system to determine the spectral type, and hence constrain the mass and temperature, of the faint companion to the AGB star. Our spectroscopic analysis puts the companion's spectral type in the range F8V–G0V. Our photometric observations broadly agree with this result and indicate that the companion undergoes extensive extinction, most likely due to dust produced by the AGB star.

Keywords: stars: AGB and post-AGB – stars: individual: W Aql – circumstellar matter – stars: mass-loss – stars: evolution – (stars:) binaries: spectroscopic – (stars:) binaries: visual

List of Appended Papers

This thesis is based on the work contained in these papers:

I. *Detailed modelling of the circumstellar molecular line emission of the S-type AGB star W Aquilae*

T. Danilovich, P. Bergman, K. Justtanont, M. Maercker, H. Olofsson, and S. Ramstedt

Astronomy & Astrophysics, submitted (2013)

II. *Classifying the secondary component of the binary star W Aquilae*

T. Danilovich, G. Olofsson, J. H. Black, K. Justtanont, and H. Olofsson

Manuscript intended for Astronomy & Astrophysics Letters

These papers are referenced in the text using their associated Roman numerals.

Contents

Abstract	i
List of Appended Papers	iii
1 Introduction	1
1.1 Stellar evolution	1
1.2 Evolution within the AGB	3
1.3 Nucleosynthesis	3
1.4 Dust and the dust-driven wind	4
1.5 Determining mass-loss rates	5
1.6 Distances to AGB stars	6
2 Radiative Transfer and Modelling	9
2.1 Molecular transitions	9
2.1.1 Linear molecules	10
2.1.2 Symmetric top molecules	10
2.1.3 Asymmetric top molecules	11
2.1.4 Spin isomers	11
2.1.5 Other considerations	11
2.1.6 Radiative rates	12
2.1.7 Collisional rates	13
2.2 Radiative transfer equations	14
2.3 Line emission modelling	15
2.3.1 The Monte-Carlo Program	16
2.3.2 The Accelerated Lambda Iteration Method	19
2.4 Dust radiative transfer	20
2.5 CSE properties	22
2.5.1 The radiation field	22
2.5.2 Velocity field	23
2.5.3 Envelope size	23

3	Observations and Data Reduction	27
3.1	Introduction	27
3.2	Herschel/HIFI	27
3.3	APEX	29
3.4	NOT	29
	3.4.1 Spectral observations	30
	3.4.2 Photometric observations	30
4	Introduction to appended papers	31
4.1	Papers I and II: W Aquilae	31
	4.1.1 Paper I	31
	4.1.2 Paper II	32
	Bibliography	35
	Acknowledgements	37
	Paper I	39
	Paper II	55

Chapter 1

Introduction

General references:

Herwig (2005); Habing & Olofsson (2003); Habing (1996)

A large portion of the radiation in the universe, with the most notable exception of the cosmic microwave background, comes from stars. Stars are ubiquitous beacons of baryonic matter and the drivers of chemical evolution in the universe. As such, the study of stellar evolution is critical to our understanding of our origin and place in the universe.

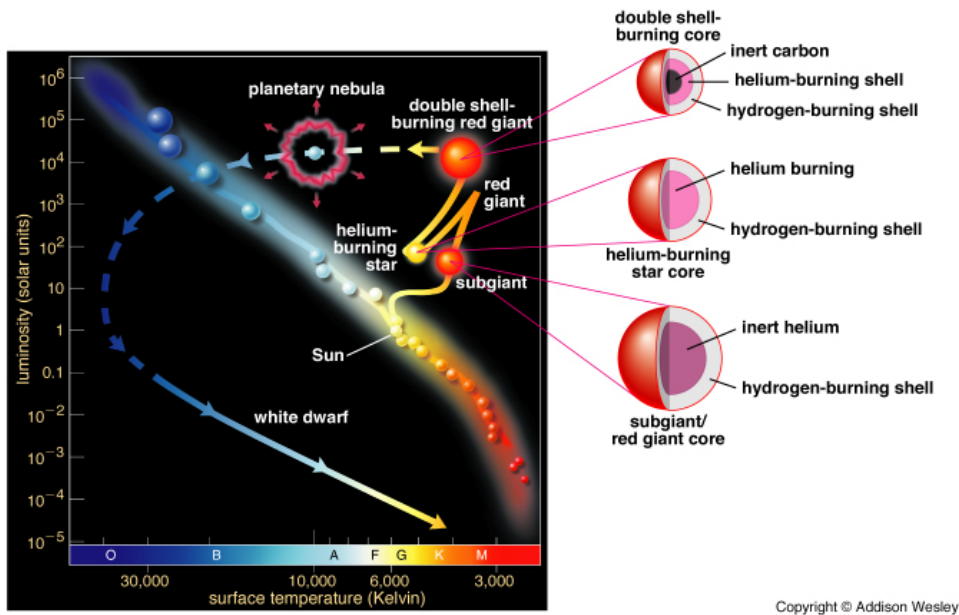
Our galaxy alone contains hundreds of billions of stars, the majority of which are of low and intermediate mass¹. These stars will eventually evolve into asymptotic giant branch (AGB) stars. AGB stars are responsible for the production of a wide variety of elements, including a selection of heavy elements not produced by main sequence stars but required, for example, for the formation of rocky planets and the evolution of life. They also contribute a significant amount of dust to the interstellar medium (ISM). The evolution of these common stars is hence of particular interest in understanding the chemical composition of the universe.

This thesis concerns itself mainly with the elements and molecules generated in and near AGB stars.

1.1 Stellar evolution

Following their tenure on the main sequence, stars of low to intermediate mass — approximately in the range $0.8\text{--}8 M_{\odot}$ — will proceed onto the asymptotic giant branch (AGB) of the Hertzsprung-Russell diagram (HR diagram, see FIG 1.1). Once such a star exhausts the hydrogen available for fusion in its core, it will ascend the red giant branch

¹Our own sun has a mass of only $1 M_{\odot}$, corresponding to 2×10^{30} kg.



Copyright © Addison Wesley

FIGURE 1.1: Hertzsprung-Russell diagram with AGB evolutionary track.

of the HR diagram, burning hydrogen only in a shell around the core. This heralds the penultimate evolutionary phase of the star. Following a brief period of helium-burning in the core, the star will ascend a second red giant branch, the Asymptotic Giant Branch, characterised by helium- and hydrogen-burning shells and a quiescent core of carbon and oxygen. This evolutionary process is roughly illustrated in FIG 1.1.

Throughout their lives, AGB stars lose mass through a combination of pulsations and radiation pressure. The ejected matter forms an expanding circumstellar envelope (CSE). There are two main types of pulsations exhibited by AGB stars. On a shorter time scale, AGB stars pulsate on a timescale of hundreds of days. They can be broadly categorised into three variability types: Mira variables, semiregular variables and irregular variables. Mira variables have a large amplitude of variability (> 2.5 magnitudes in the V band) and a regular period, semiregular variables have a smaller amplitude (< 2.5 mag in the V band) and exhibit some periodicity, while irregular variables are not known to exhibit regular variability. These pulsations contribute to the regular mass-loss of AGB stars (for more information see §1.4 discussing the dust-driven wind).

Thermal pulses are comparatively major events in the lives of AGB stars. These occur with a periodicity of 10^4 – 10^5 years and may involve the ejection of a large amount of matter, which can be characterised as a short period of intense mass-loss before returning to the pre-thermal pulse mass-loss rate. The ejecta from a thermal pulse forms a “detached shell” around the AGB star as it expands. This is distinct from the CSE

formed during prolonged periods of near-constant mass-loss. Thermal pulses are due to brief periods of explosive helium-burning during the double-shell burning phase.

Eventually, the star will eject all the mass possible, leaving behind a carbon/oxygen core, in which further nuclear-burning processes will not ignite, surrounded by the ejecta as the star moves through the post-AGB phase. The ejecta forms a planetary nebula around the stellar remnant, which becomes a white dwarf.

There is some debate as to whether all AGB stars become planetary nebulae and whether the existence of a binary companion plays an important role in the formation of the — often geometrically complicated — planetary nebula. However, such discussion is beyond the scope of this thesis.

1.2 Evolution within the AGB

Initially, a star appearing on the AGB will be an oxygen-rich M-type star, with a higher abundance of oxygen than carbon, as in our sun. Whether or not it ends its life as an M star depends strongly on its initial mass. To transition to a carbon star, the initial mass must be in the range $\sim 1\text{--}4 M_{\odot}$.

One of the most important factors that determines chemical evolution throughout the AGB phase, is the convective mixing process known as dredge-up, a process which changes the surface composition of the star. By the time a star has arrived on the AGB, it has already undergone two distinct dredge-up processes. Further evolution is governed by the third dredge-up, a potentially repeated event. The third dredge-up brings nucleosynthesis products of the H- and He-burning shells to the surface. Important products include C and s-process elements, enhancing the surface abundances of these elements. The C/O ratio increases with each third dredge-up event, evolving the star first to an S star with $C/O \sim 1$ and then to a carbon star with $C/O > 1$. Above $4 M_{\odot}$, the produced carbon is destroyed in a process called hot-bottom burning (see below) and below about $1 M_{\odot}$ the carbon production is inefficient. Hence, no C-type AGB stars are formed outside of this mass range.

1.3 Nucleosynthesis

Nucleosynthesis through fusion is limited to H and He burning in AGB stars, although super-AGB stars ($8\text{--}10 M_{\odot}$) may be massive enough to initiate C burning. These, however, are beyond the scope of this thesis.

Massive AGB stars, above $\sim 4 M_{\odot}$, will experience hot-bottom burning, where the H-burning shell has access to other elements mixed in, through convection, from outer layers. Hot-bottom burning prevents or stalls C star formation by converting the C



FIGURE 1.2: The AGB star Mira captured in a UV scattered light mosaic by the Galaxy Evolution Explorer (GALEX). The long tail is composed of matter from the CSE being left behind as Mira moves rapidly through space. *Image credit: NASA/JPL-Caltech/C. Martin (Caltech)/M. Seibert(OCIW)*

formed in the He-burning shell into N. It is expected that the S stars examined in the appended papers will not go through hot-bottom burning.

The slow neutron capture process, abbreviated to *s*-process, occurs in AGB stars and is responsible for the production of about half of all elements heavier than Fe. It is these *s*-process elements, dredged up into the star's photosphere, that give S stars their classification from optical spectra due to the appearance of molecules like ZrO.

1.4 Dust and the dust-driven wind

We know dust is present in the circumstellar envelopes of AGB stars primarily because we detect it in observations, particularly in infrared spectra such as those observed by IRAS and ISO, and through direct imaging, such as with Herschel/PACS. In FIG 1.2 the CSE of Mira has been imaged in UV scattered light and an extended trail of its CSE can be seen as Mira moves rapidly through the ISM.

Dust condenses around AGB stars out of the gas lifted to sufficiently high altitude in the stellar atmosphere. It can form only at distances from the star where the temperatures are lower than the dust grain melting point. For silicate grains, the maximum dust condensation temperature is approximately 1000 K and for amorphous carbon grains it is approximately 1500 K.

The presence of dust is important to the evolution of AGB stars. Radiation pressure on dust grains drives the mass-loss when the momentum gained by the grains is transferred through collisions to the gas molecules (Kwok, 1975; Höfner, 2011). This is known as a dust-driven wind and is thought to be the foremost mechanism for (the least intense) mass-loss in AGB stars.

The velocity of the stellar wind can be seen clearly in the width of observed circumstellar molecular emission lines and is known to vary significantly between AGB

stars, ranging up to $\sim 30 \text{ km s}^{-1}$ (Ramstedt et al., 2009). As may be naïvely assumed, there is a correlation between the wind velocity and the mass-loss rate of an AGB star, however it is not a tight correlation, as shown by Ramstedt et al. (2009). They also show a similar loose correlation between mass-loss rate (or wind velocity) and period length, indicating that longer-period variables are, in general, losing mass more rapidly.

Mass-loss is a defining characteristic of AGB stars. AGB stars rapidly lose a lot of mass, with mass-loss rates ranging from $\sim 10^{-8}$ to $10^{-4} M_{\odot} \text{ yr}^{-1}$ at various stages and depending on the parameters of the star. This rapid mass-loss dominates the evolution of the star and will eventually terminate it, as indefinite mass-loss cannot be sustained. Furthermore, the mass-loss is rapid enough to prevent the core mass from exceeding the Chandrasekhar mass, which would otherwise lead to a thermonuclear supernova explosion.

1.5 Determining mass-loss rates

Determining the mass-loss rates of AGB stars is a crucial component in their study. Knowledge of the mass-loss rates allows for estimation of the enrichment of the ISM and the lifetime of the star on the AGB. It is also an important component in the study of extragalactic stellar populations and the chemical evolution of galaxies, including at high redshifts. As such, it is crucial that mass-loss rates are determined with accuracy.

Several methods exist for determining mass-loss rates, of varying degrees of complexity and reliability. The method used in this thesis is CO line emission radiative transfer modelling, one of the most reliable methods (Ramstedt et al., 2008). The main disadvantages of using (solely) CO to determine mass-loss rates are that a CO abundance has to be assumed to convert from CO mass-loss rate to total mass-loss rate, and that at high mass-loss rates (exceeding $\sim 10^{-5} M_{\odot} \text{ yr}^{-1}$), CO becomes an unreliable estimator due to optically thick line emission and significant CO line cooling in the studied objects, both of which reduce the sensitivity of CO line intensities to the mass-loss rate. On the other hand, CO radiative transfer modelling has been used to identify recent changes in mass-loss rates in extreme OH/IR stars (Justtanont et al., 1996; Lombaert et al., 2013), which typically have high mass-loss rates.

Mass-loss rates can also be determined from a combination of dust radiative transfer modelling and modelling of the dust and gas dynamics of the star. As discussed in Ramstedt et al. (2008), this does not suffer from the same limitations as CO line radiative transfer modelling, but still rests on a number of uncertain assumptions and a relatively simple model of the dust-driven wind. When comparing this method to the results of a CO line model for the same stars, Ramstedt et al. (2008) found that the two methods were in agreement to within a factor of ~ 3 .

Several formulae for determining mass-loss rates from observed line intensities have been derived (Knapp & Morris, 1985; Loup et al., 1993; Ramstedt et al., 2008; De Beck

et al., 2010). These formulae combine a set of stellar parameters, of varying precision, and attempt to predict a mass-loss rate based on one or more CO line observations. In general these sorts of formulations are less reliable — or are reliable only over a limited range of conditions — than the more detailed modelling methods mentioned above. They do have the benefit of being considerably more expedient to compute, however, particularly as a first estimate of the mass-loss rate.

1.6 Distances to AGB stars

It is a non-trivial matter to measure the distances to AGB stars. In general, the parallax method is often used to measure stellar distances. This involves measuring the parallax shift of the star in question at different intervals along the Earth’s orbit around the Sun. The parallax method is limited by how accurately shifts in stellar positions can be measured.

Hipparcos² was an ESA mission launched in August 1989 to measure and catalogue stellar parallaxes with greater accuracy than is possible from the ground. It remains the gold standard for astrometry measurements. However, due to the variable (and dust-shrouded and extended) nature of AGB stars, Hipparcos results can be unreliable and, for more distant AGB stars, non-existent. In these cases other astrometric methods must be employed. On a star-by-star basis, masers (which are convenient point sources but which are not present in all AGB stars) can be used to obtain more accurate measurements using the parallax method as discussed in Vlemmings & van Langevelde (2007). On a more general scale, there exists a relationship between the pulsation periods of Mira variables and their luminosities. As luminosity is directly related to absolute magnitude, it is then possible to derive a distance by comparing the apparent magnitude of the star with the predicted absolute magnitude.

It is also possible to measure distances to some AGB stars using the phase lag method described by van Langevelde et al. (1990). This method can only be used on stars with significant masering — for example, OH/IR stars with strong OH masers are good candidates. The maser peak intensities vary based on the radiation field and, by monitoring the masers in these stars, a lag between the changes in intensity of the peaks corresponding to the front and rear portions of the maser shell can be seen. Since the lag corresponds to the time taken for light to travel across the shell, it can be used to measure the size of the shell, which can then be compared with the (otherwise measured) angular size and used to determine a distance to the star.

In the appended papers, the distances to Mira variables are calculated from the Mira period-magnitude relation determined by Whitelock et al. (2008):

$$M_K = \rho (\log P - 2.38) + \delta \quad (1.1)$$

²High Precision Parallax Collecting Satellite

where M_K is the K-band absolute magnitude, ρ is the slope of the period-luminosity relation, P is the period and δ is the zero point. We implement $\rho = -3.51 \pm 0.20$, $\delta = -7.52 \pm 0.07$ as Whitelock et al. (2008) found for O-rich galactic Miras. The calibration they obtained for carbon stars had higher uncertainties but was otherwise consistent with the O-rich result. This and the fact that they include some S stars in their ‘‘O-rich’’ calibration gives us no reason to expect a different period-magnitude relation to apply to S stars. The distance is then found by comparing the derived absolute magnitude with the observed apparent magnitude

$$D = 10^{(m_K - M_K)/5+1} \quad (1.2)$$

giving D in pc. If needed, this formula can also be applied to long-period semi-regular variables (and, indeed, are included in Whitelock et al.’s (2008) calibration), while a similar relation with a different slope can be used for short-period semi-regular variables, as discussed in Bedding & Zijlstra (1998).

Since it is non-trivial to convert K-band absolute magnitude to the bolometric magnitude required to calculate luminosity, we used another formulation to obtain bolometric luminosity, namely the period-luminosity relation calibrated by Glass & Evans (1981)

$$M_{\text{bol}} = 0.76 - 2.09 \log P. \quad (1.3)$$

The luminosity can then be calculated from

$$M_{\text{sun}} - M_* = 2.5 \log \frac{L_*}{L_{\odot}} \quad (1.4)$$

so that, using $M_{\text{sun}} = 4.83$ mag (and is not to be confused with M_{\odot} , the solar mass),

$$\frac{L_*}{L_{\odot}} = 42.5 P^{0.836} \quad (1.5)$$

gives the luminosity of a Mira variable in solar luminosities.

Radiative Transfer and Modelling

Astronomy is relatively unique among the sciences in that we are only able to examine the objects we study from a vast distance, especially in the case of objects which lie outside the solar system, and are unable to directly perform experiments on them. Essentially, everything we know about distant stars¹, we have inferred from observations of electromagnetic radiation.

Electromagnetic radiation is created and transformed through baryonic matter interactions. It can be emitted, absorbed or deflected, depending on the circumstances. By comparing our observations to theories, we can make inferences as to how and what caused the radiation we see. In the case of AGB stars, it is the transport of radiation through the circumstellar envelope, and its eventual emission, that is of relevance to the work presented in this thesis.

In this chapter, first the origin of molecular emission lines will be discussed, followed by the theory of radiative transfer, and finally the implementation of radiative transfer and related processes in our numerical codes.

2.1 Molecular transitions

General references:

Atkins & Friedman (1997); Hartquist & Williams (1998); Draine (2011)

Molecular emission lines are the primary basis of this thesis. Through observations of the radiation that specific molecules emit — at specific wavelengths due to their unique quantum states — we can deduce properties of not only the molecule in question, but of the rest of the gas in the CSE and of the star itself.

¹That is, significantly more distant than 1 AU, the average distance between Earth and the Sun, equal to about 1.5×10^{11} m.

Molecules can be excited in three different ways: electronically, vibrationally and rotationally. In the regime we are interested in, we can discount electronic excitation as those transitions require stronger radiation fields and higher gas temperatures than are found in AGB circumstellar envelopes.

Vibrational excitations involve bending and stretching the bonds between atoms within the molecules. The available modes of vibrational excitation depend strongly on the structure of the molecule in question. For example, a diatomic linear molecule such as CO will only have one vibrational mode of excitation: stretching along its single bond. A slightly more complex molecule such as the V-shaped H₂O, however, has three vibrational modes: bending, symmetric stretching (both H atoms moving in concert towards or away from the O atom) and antisymmetric stretching (the H atoms moving in opposite directions relative to the O atom).

The final, and least energetic, form of molecular excitation is rotational. The energy level diagram and allowed radiative transitions differ in form based mainly on the geometric shape of the molecule. The simplest molecules are linear and more complex molecules may be symmetric or asymmetric tops. We will describe the rotational energy level structure below, as the lines we observe are exclusively rotational lines.

2.1.1 LINEAR MOLECULES

For a simple linear molecule, there is only one rotational quantum number, J , and radiative transitions can occur from $J \rightarrow J \pm 1$. This is also true when the molecule is vibrationally excited. A change in vibrational energy level is not possible without a corresponding change in J of ± 1 . CO, HCN and SiO are molecules which behave in this way.

For linear molecules, only one vibrational quantum number is needed, generally denoted v , and transitions with $\Delta v = 1$ are much stronger than those with $\Delta v > 1$.

2.1.2 SYMMETRIC TOP MOLECULES

Symmetric top molecules have one axis of rotational symmetry and hence two rotational degrees of freedom. NH₃ is such a molecule. Only two rotational angular momentum quantum numbers are required to describe the rotational energy levels of a symmetric top molecule. These are usually denoted J , related to the total angular momentum, and K , related to the projection of the angular momentum along the axis of symmetry. The moments of inertia of the other two axes are equal.

The quantum numbers for a symmetric top molecule are written J_K , where K can take integer values between $-J$ and $+J$. For a given $J \neq 0$, the energy states for $K = \pm|K|$, $K \neq 0$ are degenerate and form a doublet of close energy levels due to inversion splitting. This hyperfine structure has not been considered for the modelling

of NH_3 described in this thesis. Allowed transitions are those which satisfy $\Delta J = \pm 1$ and $\Delta K = 0$.

2.1.3 ASYMMETRIC TOP MOLECULES

For molecules with no axis of symmetry, such as H_2O , three quantum numbers are required to define each energy level as there are three degrees of rotational symmetry. The rotational quantum numbers are $J(K_a, K_c)$ also written J_{K_a, K_c} . J is related to the total rotational angular momentum and K_a and K_c are, in the case of H_2O , related to the projections of the angular momentum on the two axes orthogonal to the dipole moment of the molecule. The allowed transitions for such asymmetric top molecules are $\Delta J = 0, \pm 1$ and $\Delta K_a, \Delta K_c = \pm 1, \pm 3, \dots, \pm n$ where $n = \text{odd}$.

2.1.4 SPIN ISOMERS

Molecules such as H_2 , H_2O and NH_3 , which have two or more identical atoms in symmetric positions, can exist in either ortho or para forms. In the ortho forms of the aforementioned molecules, the H nuclei all have parallel spins, giving an overall odd spin. In the para forms, one of the the H spins is antiparallel to the other(s), giving a total even spin.

The conversion of molecules between their ortho and para forms is forbidden and so the two states can be treated as separate molecules for the purposes of our modelling.

For H_2O , the ortho and para forms can be more rigorously defined by the quantum numbers. If $K_a + K_c + \nu_3 = \text{odd}$, where ν_3 is the antisymmetric stretching vibrational mode, then the molecule is in an ortho state. If $K_a + K_c + \nu_3 = \text{even}$, then it is a para state. For each J state, there is a total of $2J + 1$ ortho and para states (Kwok, 2007). The allowed transitions for H_2O , in light of ortho and para isomers, are as previously stated for asymmetric top molecules, with the caveat that K_a and K_c must either both change or both stay constant. Having $\Delta K_a = 0$ while $\Delta K_c \neq 0$, or vice versa, is not allowed.

2.1.5 OTHER CONSIDERATIONS

SPIN-ROTATION STRUCTURE OF CN

CN is a special case among our molecules of interest as it is a radical, i.e. it has an unpaired electron. As such, there is a strong interaction between the electron spin and the molecular rotation (Penzias et al., 1974). Due to this, the rotational energy levels of CN (labelled N) above the ground state are each split into two J levels (the spin-rotation structure where $J = N + S$ with $S = \frac{1}{2}$, the electron spin), which in turn are split into two or three hyperfine levels. However, hyperfine splitting for CN was not included in our modelling.

HYPERFINE STRUCTURE

Hyperfine splitting occurs due to interactions between non-zero nuclear spins and the electronic and rotational angular momentum in a molecule. For example, N causes such hyperfine splitting in the case of HCN. This is included in our modelling.

INVERSION LINES OF NH₃

NH₃ is a triangular pyramidal molecule with the N atom forming the apex of the pyramid and the three H atoms the base. The N atom is able to tunnel through the plane of the H atoms, which is known as an inversion transition. For inversion transitions, $\Delta J = 0$ and $K \rightarrow -K$.

l-TYPE DOUBLING IN HCN

The counterpart of electronic Λ -doubling, *l*-type doubling is the splitting of a vibrational state due to rotational effects. In a linear polyatomic molecule such as HCN, the bending mode changes the shape of the molecule — making it not entirely linear (Watson, 2001; Mohamed, 2005). The interaction between the resulting vibrational angular momentum and the rotational angular momentum leads to a “doubling” of the vibrational mode into (in the case of HCN) two vibrational levels. Hence the HCN (010) 14 μm bending mode splits into (01^{1c}0) and (01^{1d}0). In the ground rotational state, the two states are degenerate and there is no splitting.

2.1.6 RADIATIVE RATES

The emission and absorption of radiation by molecules of interest plays an important part in radiative transfer analyses (see §2.2). The spontaneous emission rate of radiation for a molecular transition $u \rightarrow l$ (with energies $E_u > E_l$) is governed by the corresponding Einstein A coefficient

$$A_{ul} = \frac{8\pi^2\nu^3}{3\varepsilon_0\hbar c^3} |\mu_{ul}|^2 \text{ s}^{-1} \quad (2.1)$$

where ν is the frequency of the radiation emitted due to the transition, μ_{ul} is the transition dipole moment, ε_0 is the permittivity of free space, $\hbar = \frac{h}{2\pi}$, where h is Planck’s constant, and c is the speed of light in a vacuum. A_{ul} can also be written in terms of B_{ul} , the rate of stimulated emission

$$A_{ul} = \frac{8\pi h\nu^3}{c^3} B_{ul} \quad (2.2)$$

since B_{ul} is defined

$$B_{ul} = \frac{|\mu_{ul}|^2}{6\varepsilon_0\hbar}. \quad (2.3)$$

Finally, the rate of stimulated absorption is proportional to its opposite, the rate of stimulated emission

$$B_{lu}g_u = B_{ul}g_l \quad (2.4)$$

where g_u is the statistical weight of the u energy level.

All three of these quantities are vital in solving the radiative transfer equation and the statistical equilibrium equations discussed in §2.2. The Einstein A coefficients are part of the molecular data that must be input into our models.

2.1.7 COLLISIONAL RATES

Transition rates between energy levels for a molecule of interest due to collisions with molecular hydrogen are needed for our radiative transfer modelling (see §2.2 for details of radiative transfer). These collisional rates are determined either theoretically (sometimes aided by experimental values of cross sections). However, often collisional rates are only available for collisions between the molecule of interest and He, whereas we require collisions with H₂ since this is by far the most abundant species. When only He rates are available, they can be scaled to approximate H₂ rates. The scale factor for a molecule X is

$$\gamma_{X-H_2} = \gamma_{X-He} \sqrt{\frac{\mu_{X-He}}{\mu_{X-H_2}}} \quad (2.5)$$

where γ_{X-H_2} and γ_{X-He} are the collision rates for H₂ and He respectively, and μ is the reduced mass of the colliding system

$$\mu_{X-Y} = \frac{m_X m_Y}{m_X + m_Y}. \quad (2.6)$$

The scale factor tends towards 1.4 for molecules much larger than He and H₂ (Schöier et al., 2005).

When collisional rates for a given molecule do not distinguish between hyperfine states, it is possible to calculate the hyperfine collisional rates assuming statistical equilibrium (Keto & Rybicki, 2010). The hyperfine rates are then given by

$$C_{J,K \rightarrow J',K'} = \frac{g(J, K)}{g(J)} C_{J \rightarrow J'} \quad (2.7)$$

where $C_{J,K \rightarrow J',K'}$ is the rate between hyperfine levels, $C_{J \rightarrow J'}$ the rate between the same J levels considered without hyperfine splitting, $g(J, K)$ the the statistical weight for the J, K hyperfine level and $g(J)$ the statistical weight for the J level without hyperfine splitting.

In general, the collisional de-excitation rates are defined

$$C_{ul} = c_{ul} n_{\text{col}} \quad (2.8)$$

where c_{ul} are the collisional rate coefficients in $\text{cm}^3 \text{s}^{-1}$ and n_{col} is the number density of the collision partner, usually H_2 , which varies throughout the CSE. The upwards collisional rates can be obtained from the de-excitation rates using

$$C_{lu} = C_{ul} \frac{g_u}{g_l} e^{-h\nu/kT_{\text{kin}}} \quad (2.9)$$

where g_u is the statistical weight of the level u .

2.2 Radiative transfer equations

General references: Mihalas et al. (1975)

When we observe molecular emission lines in the direction of AGB stars, what we are seeing is the result of radiation transported throughout the circumstellar envelope. As radiation propagates through a medium it will interact, undergoing absorption, emission and scattering processes. In particular, we are interested in molecular spectral lines, and although most of these equations are applicable generally, when discussing transitions below it is assumed that they are bound-bound molecular transitions within an N -level molecule.

The radiative transfer equation for radiation of frequency ν (corresponding to transition $u \rightarrow l$) propagating a distance ds , in terms of the specific intensity I_ν , is

$$\frac{dI_\nu}{ds} + \kappa_\nu I_\nu = j_\nu \quad (2.10)$$

where j_ν is the emission coefficient, which gives the local emission for the transition $u \rightarrow l$ and is given by

$$j_\nu = \frac{h\nu}{4\pi} n_u A_{ul} \phi_\nu, \quad (2.11)$$

where n_u is the level population of level u , that is, the number density of molecules with energy at level l , and ϕ_ν is the normalised Doppler profile (line shape). The absorption coefficient, κ_ν , is given by

$$\kappa_\nu = \frac{h\nu}{4\pi} (n_l B_{lu} - n_u B_{ul}) \phi_\nu. \quad (2.12)$$

The source function can now be defined

$$S_\nu \equiv \frac{j_\nu}{\kappa_\nu} = \frac{n_u A_{ul}}{n_l B_{lu} - n_u B_{ul}}. \quad (2.13)$$

Using the Einstein relations, we can rewrite this as

$$S_\nu = \frac{2h\nu^3}{c^2} \left(\frac{g_u n_l}{g_l n_u} - 1 \right)^{-1}. \quad (2.14)$$

If we define optical depth measured along ds as

$$d\tau_\nu \equiv \kappa_\nu ds, \quad (2.15)$$

we can write (2.10) in integral form

$$I_{\nu, \text{em}} = I_{\nu, \text{bg}} e^{-\tau_\nu} + \int_0^{\tau_\nu} S_\nu(\tau'_\nu) e^{-(\tau_\nu - \tau'_\nu)} d\tau'_\nu, \quad (2.16)$$

where $I_{\nu, \text{em}}$ gives us the radiation emerging from the medium, and $I_{\nu, \text{bg}}$ is the contribution from the background radiation entering the medium.

If we know the level populations, it is possible to solve the radiative transfer equation (2.10) exactly. The difficulty, of course, lies in the non-trivial problem of solving for the level populations. It is simpler in the case of local thermal equilibrium (LTE) but this is not applicable to CSE environments. Instead, we assume statistical equilibrium.

The statistical equilibrium system of equations for a transition $u \rightarrow l$ is

$$\begin{aligned} \sum_{l < u} [n_u A_{ul} - (n_l B_{lu} - n_u B_{ul}) \bar{J}_{ul}] - \sum_{l \geq u} [n_l A_{lu} - (n_u B_{ul} - n_l B_{lu}) \bar{J}_{ul}] \\ + \sum_{u, l} (n_u C_{ul} - n_l C_{lu}) = 0 \end{aligned} \quad (2.17)$$

where C_{ul} are the collisional transition rates (see §2.1.7) and \bar{J} is the integrated mean intensity averaged over all directions μ

$$\bar{J} = \frac{1}{4\pi} \int d\Omega \int d\nu \phi_\nu(\mu) I_\nu(\mu) \quad (2.18)$$

where $I_\nu(\mu)$ is the specific intensity along direction μ and $\phi_\nu(\mu)$ is used as a weight function.

As discussed further in §2.3, both of the codes we use to compute our models solve equations (2.16) and (2.17). However, it is not possible to solve (2.17) analytically so both codes use iterative methods. MCP (see §2.3.1) uses the Monte-Carlo method and ALI (see §2.3.2) uses the accelerated lambda iteration method.

2.3 Line emission modelling

We use two different codes to model the line emission in our CSEs. The Monte-Carlo Program (MCP) is used for most of our molecular modelling, most crucially for CO. As well as computing level populations, it solves the energy balance equation to find a radial kinetic temperature profile. However, MCP cannot practically be used to model H₂O, due to the high optical depth effects associated with H₂O molecules in AGB CSEs, even

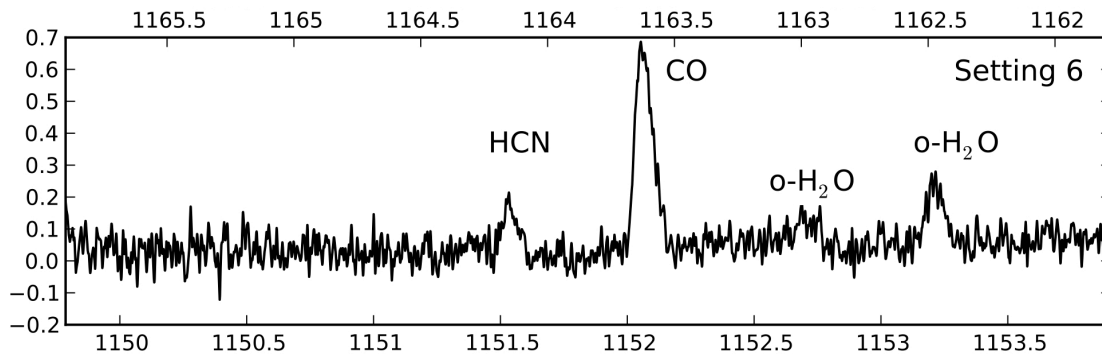


FIGURE 2.1: A HIFI spectrum showing four molecular emission lines from the HIFISTARS Programme (see §3.2 for more details). Both upper- and lower-sidebands are plotted with the upper horizontal axis giving the frequency in GHz for the upper sideband and the lower horizontal axis giving the frequency in GHz for the lower sideband. These emission lines are extracted from the spectrum and compared with our model emission lines.

for S stars. Hence, to model H_2O we use the Accelerated Lambda Iteration Program (ALI). Although ALI can be used to model any well-defined molecule in the CSE, the version we use in Paper I does not solve the energy balance equation so we maintain the use of MCP for CO modelling. We also used MCP for the other molecules modelled in Paper I as it is less computationally demanding.

Any line modelling is preceded by a dust radiative transfer model to calculate the radiation field emitted by the dust and to obtain the dust parameters required as input in MCP and ALI. This is discussed in §2.4.

In FIG 2.1 we show an example of an observation that our line model would be compared to. Where possible (and especially for CO) our line models would always be compared with as many observed molecular lines as possible.

2.3.1 THE MONTE-CARLO PROGRAM

Our MCP has been previously described in Schöier & Olofsson (2001); Schöier et al. (2002); Ramstedt et al. (2008) and is based on pioneering work by Bernes (1979). Benchmarking comparisons have been made in van Zadelhoff et al. (2002) between MCP and other radiative transfer codes and methods, showing that MCP produces good agreement with other results.

The Monte-Carlo method² simulates a number of model photons, each of which represents a group of real photons from all the transitions under consideration. The photons are followed through the CSE and their absorptions and emissions are tracked.

²The Monte-Carlo method as distinct from the Monte-Carlo Program, MCP, which implements both the Monte-Carlo method as well as non-Monte-Carlo elements.

A major disadvantage of the Monte-Carlo method is the computing time needed to lower the random errors inherent in the method (the MC noise). The decrease in MC noise is inversely proportional to the square root of the number of simulated photons and increasing the number of photons increases the MCP runtime significantly. For similar reasons, the Monte-Carlo method is not adept at modelling high optical depths. If the optical depth of the molecular lines is sufficiently high, it is possible that all the model photons will be absorbed before they can reach all parts of the CSE, giving erroneous results. This optical depth problem can be diminished by introducing a larger number of model photons, but then the computing time becomes unwieldy.

An advantage of the Monte-Carlo method is the ease with which non-regular grids can be implemented. This means that, for example, in the denser inner regions of a CSE where conditions are changing rapidly, more grid points can be placed than in the outer regions, instead of forcing the grid points to be placed with regular logarithmic spacing.

One iteration of our MCP ends when, governed by the statistical equilibrium equation (2.17), all the photons have either been absorbed in the CSE or have escaped. After a set number of iterations in which only the level populations are adjusted, the code begins to adjust the temperature profile with each iteration as well.

This is the main advantage of using MCP; that it (analytically) solves the energy balance equation (Groenewegen, 1994)

$$\frac{dT}{dr} = (2 - 2\gamma) \left(1 + \frac{r}{2v(r)} \frac{dv}{dr} \right) \frac{T_{\text{kin}}(r)}{r} + \frac{\gamma - 1}{n_{\text{H}_2}(r) k_B v(r)} (H - C) \quad (2.19)$$

where T_{kin} is the kinetic temperature of the gas, $n_{\text{H}_2}(r)$ is the hydrogen number density, k_B is Boltzmann's constant, γ is the adiabatic index with $\gamma = \frac{5}{3}$ for $T_{\text{kin}} < 350$ K and $\gamma = \frac{7}{5}$ otherwise, and H and C are the sums of the heating and cooling terms respectively. The adiabatic cooling term for an accelerating wind is given by the first term on the right-hand side of the equation.

MCP adjusts the temperature profile with each iteration and recalculates the level populations using the new temperature profile each time. As many of the heating and cooling terms (described below) depend either on the kinetic temperature, level populations or both, the iterative changes allow MCP to gradually converge to a solution.

The heating processes included in MCP and their formulations are:

- Dust-gas collisional heating (Schöier & Olofsson, 2001)

$$H_{dg}(r) = \frac{3}{8} m_{\text{H}_2}^2 n_{\text{H}_2}(r)^2 \frac{\Psi}{a_g \rho_g} \frac{v_{\text{drift}}^3}{\left(1 + \frac{v_{\text{drift}}(r)}{v(r)} \right)} \quad (2.20)$$

where m_{H_2} is the mass of an H_2 molecule, Ψ is the dust-to-gas mass ratio, $a_g = 0.1 \mu\text{m}$ is the average dust grain size, and $\rho_g = 3.3 \text{ g cm}^{-3}$ is the dust grain density (for silicate dust). This is the most important heating process in most parts of the CSE.

- Non-collisional interactions between dust and gas (for example the temporary adhesion of a molecule to a dust grain; Groenewegen, 1994)

$$H_{dt}(r) = 2.008 \times 10^{-31} n_{\text{H}_2}(r)^2 \frac{\Psi}{\rho_g a_g} \sqrt{T_{\text{kin}}(r) (T_{\text{dust}}(r) - T_{\text{kin}}(r))} \left(0.35 \exp \left(-\sqrt{\frac{T_{\text{dust}}(r) + T_{\text{kin}}(r)}{500}} \right) + 0.1 \right) \quad (2.21)$$

- Photoelectric heating (Huggins et al., 1988)

$$H_{\text{pe}} = K_{\text{pe}} n_{\text{H}_2}(r) \quad (2.22)$$

with $K_{\text{pe}} = 10^{-26} \text{ erg s}^{-1}$,

- Line heating, which occurs as a result of negative line cooling

The cooling processes included in MCP are:

- H_2 vibrational line cooling

$$C_{\text{H}_2}(r) = 2.611 \times 10^{-21} n_{\text{H}_2}(r) \left(\frac{T_{\text{kin}}(r)}{1000} \right)^{4.74} \quad (2.23)$$

- CO rotational line cooling, which follows Sahai's (1990) formulation,

$$C_{\text{CO}}(r) = \sum_{u, u>l} \Delta E_{ul} k_B (n_l C_{lu} - n_u C_{ul}) \quad (2.24)$$

where n_u is the population of level u , C_{ul} is the collisional excitation rate from u to l , ΔE_{ul} is the difference in energy between rotational levels u and l , and k_B is Boltzmann's constant.

It is also possible to include additional line cooling due to H_2O or HCN , which is calculated in the same manner as the CO cooling. Further, it is possible in some circumstances for the CO line cooling to act as heating and for the H_{dt} term to act as cooling, depending on the conditions in regions of the CSE.

After determining the temperature structure from the CO line modelling, other molecules such as SiO , HCN and NH_3 , and isotopologues such as ^{13}CO can be modelled using the temperature and mass-loss rate solution obtained from the CO line modelling.

When modelling CO lines, we assume a CO fractional abundance relative to H_2 (which is 6×10^{-4} for S stars) and the parameters that are adjusted to match the observed lines are mass-loss rate, \dot{M} , and dust-to-gas ratio, Ψ . The latter plays a role in the two dust-related heating terms and has an effect on the energy transport throughout

the envelope. As such, adjusting Ψ affects the line intensity ratios between different transitions. A larger Ψ will, in general, increase the intensity of the high- J transition lines ($J \gtrsim 3$) and decrease the central intensity of the low- J lines while making them more strongly double-peaked. A smaller Ψ will have the opposite effect, decreasing the high- J lines and increasing the intensities of the low- J while making them more parabolic.

When modelling line emission from molecules other than ^{12}CO , only one parameter is adjusted to fit the observed lines: the fractional abundance of the molecule.

2.3.2 THE ACCELERATED LAMBDA ITERATION METHOD

The ALI method has been previously described in Rybicki & Hummer (1991) and reviewed in detail by Hubeny (2003). Its application to CSE line emission used here has been described and tested in Maercker et al. (2008, 2009) and Schöier et al. (2011). Benchmarking by Maercker et al. (2008) shows that it performs as well as other radiative transfer codes and methods.

Like MCP, the ALI method solves the statistical equilibrium equations (2.17). Its name comes from the introduction of the lambda operator, an $N \times N$ matrix for N radial points, defined by

$$I_\nu(\mu) = \Lambda_{\mu,\nu} S_{\nu, \text{tot}}(\mu) + I_{\text{bg}} \quad (2.25)$$

where $S_{\nu, \text{tot}}(\mu)$ is the global source function. It is similar to the transition source function S_ν in (2.13), but includes the dust component and any overlapping lines.

The diagonal components of $\Lambda_{\mu,\nu}$ give the local contributions to \bar{J} (see (2.18) for the definition), and the off-diagonals give the non-local contributions. The ‘‘accelerated’’ part of the ALI method comes in from splitting the operator so that high optical depths are computed separately, making the code converge much more quickly at high optical depths than it would otherwise. The ALI code is used to model H_2O because H_2O lines can have particularly high optical depths. Also, many H_2O transitions can become strong masers (for example, the famous 22 GHz water maser line) and ALI can handle these cases as well. The main disadvantage with our code is that the model needs to converge to some extent before the lambda acceleration can be ‘‘turned on’’ (ditto the Ng acceleration (Ng, 1974) which is also implemented in our ALI code). This means that the ALI code can be slow to begin converging, depending on the specific model parameters, but once the accelerations are initiated, it generally converges in a small number of iterations.

The version of ALI used in Paper I does not include the energy balance equation but does calculate the molecular line cooling for the final level population distribution of the molecule in question. The ideal modelling method for stars for which we have H_2O and CO lines (and potentially other molecules also) is as follows:

1. Run an SED model to determine the radiation fields (see §2.4)

2. Using results from the SED model (particularly the stellar temperature and the dust properties), run MCP for CO and find a model which fits the observed lines reasonably well (it does not have to be the most precise best-fit model at this stage)
3. Using SED and MCP results (notably the temperature profile and mass-loss rate from MCP) run ALI for H₂O and find a model which fits the H₂O lines reasonably well. The ALI model will output an H₂O cooling function of the same form as (2.24).
4. Use the H₂O cooling term obtained from ALI in the MCP CO model, and run until a good fit is found for the CO lines
5. Iterate steps 3 and 4 until a consistent and convergent model is found for the CO and the H₂O lines.

However, there are problems with following this method. The cooling due to H₂O is often so large in the inner part of the CSE so that for some models there is more cooling than heating, leading to unphysical results. Even in our best fit models using this method, the results were rarely stable. A possible “solution” to find a stable model is to increase the gas-dust collisional heating by using a larger dust-to-gas ratio or increasing the drift velocity. Using a constant drift velocity, instead of a drift velocity profile as discussed in §2.5.2, increases the degree of heating in the inner envelope, which is the region where problems with H₂O cooling arose. However, both of these adjustments have other consequences on the goodness of fit and, furthermore, such models were not pursued further giving the large number of uncertainties present.

Instead of the process described above, we decided to not include H₂O cooling in the MCP energy balance in Paper I. Our final results include ALI models for H₂O but do not include the water cooling predicted by them.

It is our goal in further work to include the energy balance equation in ALI so that we can create more accurate H₂O models.

2.4 Dust radiative transfer

To model the radiative contributions from the dust in the CSE, we used a spectral energy distribution (SED) model that implements silicate dust (Justtanont & Tielens, 1992) and is based on the method described in Haisch (1979). We input the following parameters into the model: distance to the star, gas terminal velocity, dust-to-gas mass ratio, dust grain density (3.3 g cm^{-3} for silicate) and dust condensation temperature (1000 K for silicate). We constrain the model with photometric observations and, where available,

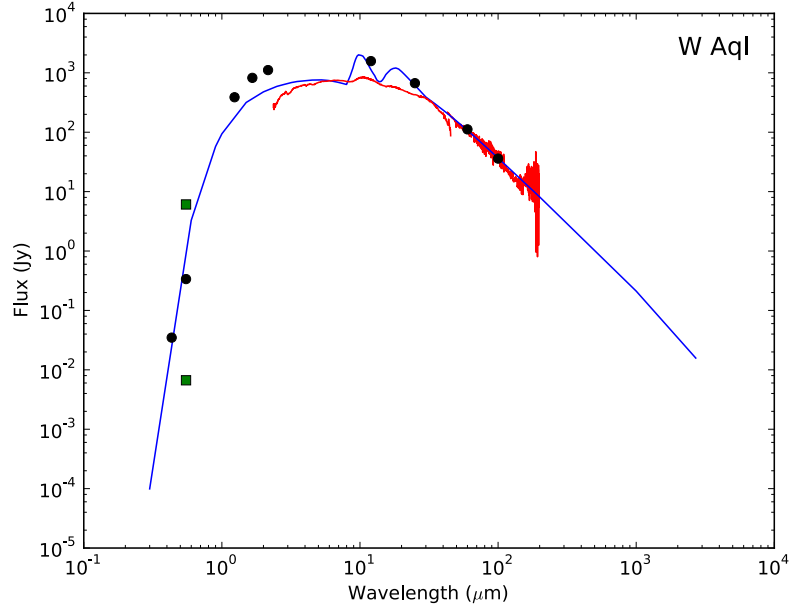


FIGURE 2.2: The SED model fit for the AGB S-type star W Aql. The model is shown in blue, the ISO SWS spectrum is shown in red, the black points are photometric measurements from 2MASS, IRAS and other sources, and the green squares show the variability in flux in the visible. For more information, see Paper I.

ISO³ and IRAS⁴ spectra, and fit the stellar temperature and dust mass-loss rate. From the model we are able to extract (as well as the parameters used in the fitting) the dust optical depth and the dust condensation radius. These parameters are later used in the line models. An example of an SED model fit to available data is shown in FIG 2.2

The dust optical depth is defined similarly to (2.15) along distance s

$$\tau_d(\nu) = \kappa_d(\nu)s \quad (2.26)$$

where κ_d is dependent on both the frequency and the type of dust.

$$\kappa_d = \frac{3}{4} \frac{Q}{\rho_s a} \quad (2.27)$$

where ρ_s is the specific density of the dust, Q is the absorption efficiency and a is the grain radius. A plot showing κ_d , also known as dust opacity, for silicate dust as used in our modelling is shown in FIG 2.3. The long wavelength tail can be approximated as a power law that continues out to longer wavelengths than shown in the plot.

The SED modelling also outputs a dust temperature profile. In Paper I we use the dust temperature profile directly in the line modelling.

³Infrared Space Observatory

⁴Infrared Astronomical Satellite

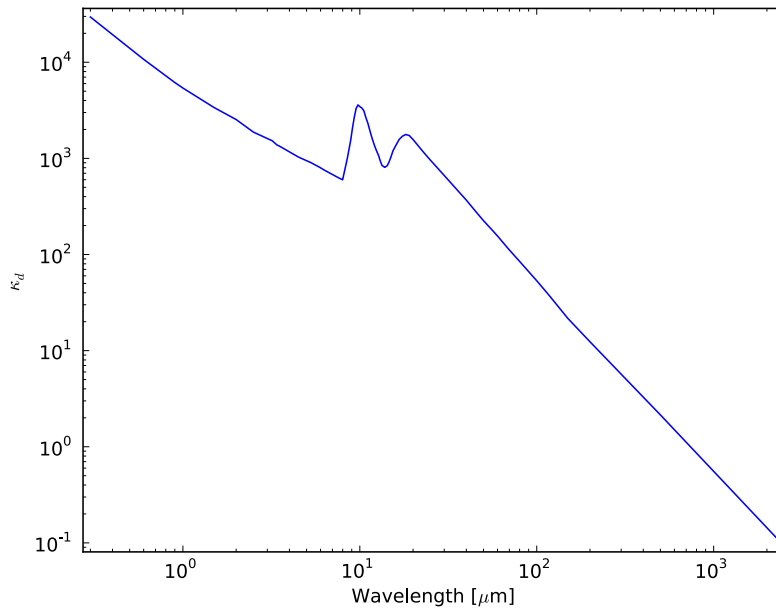


FIGURE 2.3: The dust opacity dependence on wavelength for silicate dust.

2.5 CSE properties

In our radiative transfer modelling we assume a spherically symmetric circumstellar envelope formed by a smoothly accelerating wind and a constant mass-loss rate. Most of the input parameters and calculations for the model CSE are independent of whether MCP or ALI are being used. These include the radiation and velocity fields, and molecular envelope sizes. The details are described below.

2.5.1 THE RADIATION FIELD

We get the radiation field affecting the CSE by combining the stellar radiation field, the dust radiation field and the radiation field due to the CMB⁵. The stellar radiation field comes from assuming the star is a black body of temperature T_{eff} , the effective stellar temperature, which is found during the SED modelling. The dust radiation field comes directly from the dust temperature profile generated in the SED modelling and for the CMB comes from assuming a constant CMB temperature of 2.7 K.

⁵Cosmic Microwave Background radiation

2.5.2 VELOCITY FIELD

We assume that the CSE has a velocity field defined by a relatively smooth acceleration. The general radial velocity law used is

$$v(r) = v_{\min} + (v_{\infty} - v_{\min}) \left(1 - \frac{R_{\text{in}}}{r}\right)^{\beta} \quad (2.28)$$

where v_{\min} is the innermost expansion velocity, v_{∞} is the terminal expansion velocity, R_{in} is the dust condensation radius as calculated in the corresponding SED model, and β is a parameter used to describe the acceleration in the inner part of the envelope.

For the gas velocity profile, $v_{\min} = 3 \text{ km s}^{-1}$ is set to the approximate speed of sound at R_{in} and v_{∞} is determined from low- J line widths. The value of β is determined by fitting to the line shapes.

The minimum drift velocity is generally taken to be 1 km s^{-1} (giving a minimum dust velocity of 4 km s^{-1}) and the terminal drift velocity can be determined in one of two ways: using a dynamical model or from the formula

$$v_{\text{drift}} = \sqrt{\frac{Lv_{\infty}Q}{\dot{M}c}} \quad (2.29)$$

where L is the luminosity, \dot{M} is the mass-loss rate, Q is an efficiency factor assumed to be 0.03, and c is the speed of light. The drift velocity profile was then calculated from (2.28) using the same β value as for the gas velocity profile. The dust velocity is then, of course, the sum of the gas and drift velocities.

For W Aql in Paper I, however, we calculated the terminal dust and drift velocities using the dynamical code described in Ramstedt et al. (2008).

2.5.3 ENVELOPE SIZE

The radial abundance distribution, for a given molecule, is primarily determined by its formation mechanism and by its photodissociation by the interstellar radiation field. It can be constrained in two ways: directly from interferometer observations, which we did not have access to, and from modelling a broad J range of high-resolution lines. The latter method, it transpires, is not as reliable as might be thought, although it is more accessible. We found that there was some degeneracy between the effects of envelope size and dust properties. Testing the effects of dust-to-gas ratio and drift velocity in the MCP code, we found that increasing or decreasing the drift velocity had a similar effect to changing the dust-to-gas ratio, as discussed in §2.3.1. The effect of increasing the dust-to-gas ratio in particular makes the low- J lines appear more double-peaked which bears a resemblance to the effect of observing an envelope which is resolved in the telescope beam. That is, unresolved emission will give a line which appears

flat on top, while resolved emission will give a more distinctly double-peaked line. The result of using a too-high dust-to-gas ratio can thus make it appear as though the modelled envelope is too large and hence predicted to be resolved. This degeneracy makes adjusting both the envelope size and the dust-to-gas ratio unreliable. Since others have come up with more reliable measurements of envelope size than presently exist for dust-to-gas ratios (or for dust or drift velocities), we have chosen not to modify the envelope size and use the prescriptions described below.

The size of the CO emitting envelope is calculated based on the equations in Schöier & Olofsson (2001) which follow the methods of Mamon et al. (1988). The radial abundance is described by

$$f(r) = f_0 \exp \left(-\ln(2) \left(\frac{r}{R_{1/2}} \right)^\alpha \right) \quad (2.30)$$

where f_0 is the central fractional abundance, and $R_{1/2}$ is the half-abundance radius determined by

$$R_{1/2} = 5.4 \times 10^{16} \left(\frac{\dot{M}}{10^{-6}} \right)^{0.65} \left(\frac{v_\infty}{15 \text{ km s}^{-1}} \right)^{-0.55} \left(\frac{f_0}{8 \times 10^{-4}} \right)^{0.55} + 7.5 \times 10^{15} \left(\frac{v_\infty}{15 \text{ km s}^{-1}} \right) \text{ cm} \quad (2.31)$$

and

$$\alpha = 2.79 \left(\frac{\dot{M}}{10^{-5}} \frac{15}{v_\infty} \right)^{0.09}. \quad (2.32)$$

The same envelope size is assumed for ^{13}CO . Indeed, where we have isotopologues and spin isomers we use consistent envelope sizes (with different central abundances).

For most of the other molecules we model, we assume a gaussian abundance distribution given by

$$f(r) = f_0 \exp \left(- \left(\frac{r}{R_e} \right)^2 \right) \quad (2.33)$$

where R_e is the e -folding radius which is determined differently for each molecule. R_e is the parameter subsequently referred to when discussing envelope size (unless $R_{1/2}$ is explicitly indicated). This abundance distribution is, to first approximation, valid for a molecule that is formed close to the star and is eventually destroyed by photodissociation in the expanding envelope.

The size of the H_2O emitting envelope is taken from Netzer & Knapp (1987). It has been tested by Maercker et al. (2009) and found to be consistent with their models. It is

given by

$$R_{\text{H}_2\text{O}} = 5.4 \times 10^{16} \left(\frac{\dot{M}}{10^{-5} M_{\odot} \text{ yr}^{-1}} \right)^{0.7} \left(\frac{v_{\infty}}{\text{km s}^{-1}} \right)^{-0.4} \text{ cm.} \quad (2.34)$$

The SiO envelope size comes from a relationship determined by González Delgado et al. (2003)

$$\log R_{\text{SiO}} = 19.2 + 0.48 \log \left(\frac{\dot{M}}{v_{\infty}} \right) \quad (2.35)$$

where R_{SiO} is in cm, \dot{M} in $M_{\odot} \text{ yr}^{-1}$, and v_{∞} in km s^{-1} .

The HCN envelope size comes from a similar relationship found by Schöier et al. (2013)

$$\log R_{\text{HCN}} = 19.9 + 0.55 \log \left(\frac{\dot{M}}{v_{\infty}} \right). \quad (2.36)$$

No such relationship exists for NH_3 as it is not as widely observed as the other molecules discussed thus far (and, indeed, it is more difficult to observe for a number of reasons). In this case we assumed the same envelope size as found for H_2O in the same star (W Aql in Paper I). This is not necessarily accurate as we know little about the behaviour of NH_3 in AGB CSEs.

The final molecule we have modelled is CN. CN is believed to be a photodissociation product of HCN and thus is not expected to have a gaussian abundance distribution (although Schöier et al. (2011) found evidence that it might). As such, we use a shell-like abundance distribution for CN following

$$f(r) = f_{\text{CN}} \exp \left(-4.6 \frac{(r - R_{\text{peak}})^2}{R_w^2} \right) \quad (2.37)$$

where f_{CN} is the peak abundance (in the shell, not at the centre of the CSE), R_{peak} is the peak radius, taken to be the same as the HCN e -folding radius, and R_w is a parameter which governs the width of the shell.

Chapter 3

Observations and Data Reduction

3.1 Introduction

All of the new data presented in Paper I came from Herschel/HIFI¹ observations conducted by the Guaranteed Time Key Programme HIFISTARS. Paper II is based on new observations taken at the Nordic Optical Telescope (NOT).

In Paper I we also use a variety of previously published archive data to supplement our new observations. Some of these, notably from the Atacama Pathfinder Experiment (APEX) archive, required basic reduction, while some were acquired in an already-reduced form. The already-reduced data include all the observations we used from the Institut de Radioastronomie Millimétrique (IRAM) 30 m telescope, the James Clerk Maxwell Telescope (JCMT), which is a 15 m dish located on Mauna Kea, Hawaii, USA, the Onsala 20 m telescope (OSO) located at Onsala Space Observatory, Sweden and the now-decommissioned Swedish-ESO 15 m Submillimetre Telescope (SEST) on La Silla, Chile.

In this chapter we briefly describe the data reduction we conducted.

3.2 Herschel/HIFI

The initial reduction of the data obtained with Herschel/HIFI was conducted in the Herschel Interactive Processing Environment (HIPE)², the Herschel data reduction pipeline software. From HIPE the data were extracted and further reduced — including efficiency and baseline corrections — using python.

The molecular transitions observed by Herschel/HIFI across all the appended papers are given in Table 3.1, which includes the half-power beamwidths and the main beam

¹HIFI is the Heterodyne Instrument for the Far-Infrared onboard the Herschel Space Observatory

²http://herschel.esac.esa.int/HIPE_download.shtml

TABLE 3.1: Molecular transitions observed by Herschel/HIFI

Molecule	Transition	Freq [GHz]	η_{mb}	θ ["]
CO	$J = 16 \rightarrow 15$	1841.345	0.70	11.5
	$J = 10 \rightarrow 9$	1151.985	0.64	18.4
	$J = 6 \rightarrow 5$	691.473	0.75	30.7
^{13}CO	$J = 10 \rightarrow 9$	1101.349	0.74	19.3
	$J = 6 \rightarrow 5$	661.067	0.75	32.1
o- H_2O	$J_{K_a, K_c} = 3_{2,1} \rightarrow 3_{1,2}$	1162.911	0.64	18.2
	$J_{K_a, K_c} = 3_{1,2} \rightarrow 2_{2,1}$	1153.127	0.64	18.4
	$J_{K_a, K_c} = 3_{1,2} \rightarrow 3_{0,3}$	1097.365	0.75	19.3
	$J_{K_a, K_c} = 1_{1,0} \rightarrow 1_{0,1}$	556.936	0.75	38.1
p- H_2O	$J_{K_a, K_c} = 1_{1,1} \rightarrow 0_{0,0}$	1113.343	0.64	19.1
HCN	$J = 13 \rightarrow 12$	1151.452	0.64	18.4
H^{13}CN	$J = 8 \rightarrow 7$	690.551	0.75	30.7
SiO	$J = 16 \rightarrow 15$	694.294	0.75	30.6
^{29}SiO	$J = 13 \rightarrow 12$	557.179	0.75	38.1
NH_3	$J_K = 1_0 \rightarrow 0_0$	572.498	0.75	37.1

efficiencies. The main beam efficiency conversion results in an intensity scale that you would measure in a lossless telescope (for a source that is equal or smaller than the main beam).

The half-power beamwidths for HIFI are given by:

$$\theta_{\text{B}}[\text{rad}] = \frac{2}{\pi}(1.6 + 0.021 \times T_e[\text{dB}])\frac{\lambda}{D} \quad (3.1)$$

where λ is the observed wavelength, the edge taper is $T_e = 7.94 \pm 0.82$ dB and the telescope diameter for Herschel is $D = 3.28$ m (Roelfsema et al., 2012). This can be written in a simpler form for easier calculation:

$$\theta_{\text{mb}}["] = \frac{21220}{\nu[\text{GHz}]}. \quad (3.2)$$

The main beam efficiencies for HIFI are given by

$$\eta_{\text{mb}} = \eta_{\text{mb},0} \exp \left[-(4\pi\sigma/\lambda)^2 \right], \quad (3.3)$$

where $\sigma = 3.8 \mu\text{m}$ is the telescope surface accuracy, and $\eta_{\text{mb},0}$ is 0.66 in HIFI band 5 (1120 – 1280 GHz) and 0.76 for all other frequencies.

TABLE 3.2: Molecular transitions of observations taken from the APEX archive

Molecule	Transition	Freq [GHz]	η_{mb}	θ ["]
CO	$J = 7 \rightarrow 6$	806.652	0.43	8
	$J = 4 \rightarrow 3$	461.041	0.60	14
	$J = 3 \rightarrow 2$	345.796	0.73	18
	$J = 2 \rightarrow 1$	230.538	0.75	27
^{13}CO	$J = 3 \rightarrow 2$	330.588	0.73	18
	$J = 2 \rightarrow 1$	220.399	0.75	28
SiO	$J = 11 \rightarrow 10$	477.505	0.60	13
	$J = 8 \rightarrow 7$	347.331	0.73	14
	$J = 5 \rightarrow 4$	217.105	0.75	28

3.3 APEX

APEX is a 12 m dish located on Llano de Chajnantor in Northern Chile at an altitude of 5100 m.

A handful of lines observed with SHeFI³ were taken from the APEX data archive and used in Paper I. The data reduction was conducted in CLASS and python. The different lines observed with APEX and used in the appended papers are given in Table 3.2 along with the half-power beam widths and the main beam efficiencies.

The half-power beam width for APEX is given by

$$\theta["] = 7.8 \frac{800}{\nu[\text{GHz}]} \quad (3.4)$$

where ν is the transition frequency.

3.4 NOT

The NOT is a 2.5 m optical telescope located in La Palma (the Canary Islands), Spain. Two different types of data were observed with the NOT and are presented in Paper II: spectral and photometric observations. Both data types were reduced using IRAF⁴. For both spectral and photometric observations we used the using the ALFOSC instrument⁵.

³The Swedish Heterodyne Facility Instrument

⁴Version 2.16, <http://iraf.noao.edu/>

⁵The Andalucia Faint Object Spectrograph and Camera

Our spectral observations were taken on two separate occasions: once when W Aql was close to maximum brightness and once when W Aql was close to minimum brightness. The photometric observations were taken only on the latter occasion.

3.4.1 SPECTRAL OBSERVATIONS

The spectral observations were obtained with Grism #7, which has 600 rules/mm, a dispersion of 1.5 Å/pixel, a central wavelength of 5260 Å and a range of 3850–6850 Å. A HeNe calibration lamp was used, in which the spectral features were identified by hand from provided charts. In IRAF, the `apall` routine was used to do the majority of the data reduction.

3.4.2 PHOTOMETRIC OBSERVATIONS

W Aql was observed in the U, B and V bands with the NOT photometric filters U_Bes 362_60, B_Bes 440_100 and V_Bes 530_80, respectively. The data were reduced with IRAF primarily using the `daophot` routine.

After reducing the data, they were used to examine various parameters of W Aql. The most important were the absolute magnitude and the slope of the extinction. The absolute magnitude is found using

$$M = m - 5 \log d + 5 \quad (3.5)$$

where m is the apparent magnitude and d is the distance.

The slope of the extinction is found using

$$R_V = \frac{A_V}{E(B - V)} \quad (3.6)$$

where A_V is the extinction in the V band (calculated relative to the expected brightness) and $E(B - V) = A_B - A_V$ is the reddening.

Introduction to appended papers

4.1 Papers I and II: W Aquilae

W Aql is a binary system at a distance of about 400 pc, containing an S-type AGB star with optical spectral classification S6/6e and a main sequence companion, which we classified in Paper II. The S star is on the more carbonaceous end of the S star spectral classification scale, just one division away from being an SC star. In Paper I we performed detailed modelling of the CSE of the AGB component.

4.1.1 PAPER I

As part of the HIFISTARS Guaranteed Time Key Project, W Aql was observed by Herschel/HIFI in nine different frequency settings. A variety of molecules were detected, including CO, H₂O, HCN, SiO and NH₃ — the latter for the first time in an S star — as well as some of their isotopologues.

In Paper I we model the conditions in the circumstellar envelope, in particular the mass-loss rate and the relative abundances of the detected molecules. We use MCP (see §2.3.1) to find the mass-loss rate through a CO model, and subsequently find the abundances for the remaining molecules except for H₂O, also using MCP. We model the two spin isomers of H₂O separately using ALI (see §2.3.2) to find their respective abundances. We find a mass-loss rate of $3.5 \times 10^{-6} M_{\odot} \text{ yr}^{-1}$ and a gas expansion velocity of 16.5 km s^{-1} .

In general we find that W Aql behaves as an S star, with some M star characteristics and some C star characteristics. When comparing line intensity ratios in W Aql and other stars observed as part of HIFISTARS, we find that in terms of H₂O line intensities, the S stars behave more like C stars, but in terms of HCN line intensities they behave more like M stars. Comparing W Aql and χ Cyg, the only other S star observed as part of HIFISTARS, we found that the main differences between the two stars were the CN

lines that are present in the χ Cyg spectrum and absent in W Aql and the NH_3 line that is detected in W Aql but not in χ Cyg. The first is a surprising result as χ Cyg is believed to be less carbon-rich than W Aql and hence it would be expected that there would be more CN present in W Aql. A more expected result was a lower abundance of SiO in W Aql than in χ Cyg, which is in line with expectations for their respective classifications.

4.1.2 PAPER II

W Aql has a binary companion at a separation of $0.46''$ (Ramstedt et al., 2011). At 395 pc, this corresponds to a minimum separation of approximately 186 AU. In Paper II we use new observations from the Nordic Optical Telescope (NOT) to classify the companion to W Aql.

We took spectral observations on two separate occasions, once when W Aql was at maximum brightness and hence the spectrum was dominated by the S star, and once when W Aql was at minimum brightness and hence the spectrum revealed features from the companion, especially at the blue end of the spectrum. From the spectral observations we find the companion to be on the main sequence, in the range F8–G0, most likely an F8 or F9 star. We also confirmed the classification of S6/6e for the S star component.

We took photometric observations of W Aql at minimum brightness and we use these to discuss the orientation of the W Aql system and the quantity of dust lying between the observer and the main sequence component. From the extinction calculated from our observations, we believe that the main sequence component lies behind the S star's circumstellar envelope, relative to our line of sight.

Bibliography

- Atkins, P. & Friedman, R. 1997, *Molecular quantum mechanics*, 3rd edn. (Oxford University Press)
- Bedding, T. R. & Zijlstra, A. A. 1998, *The Astrophysical Journal Letters*, 506, L47
- Bernes, C. 1979, *Astronomy & Astrophysics*, 73, 67
- De Beck, E., Decin, L., de Koter, A., et al. 2010, *Astronomy & Astrophysics*, 523, A18
- Draine, B. 2011, *Physics of the Interstellar and Intergalactic Medium*, Princeton Series in Astrophysics (Princeton University Press)
- Glass, I. S. & Evans, T. L. 1981, *Nature*, 291, 303
- González Delgado, D., Olofsson, H., Kerschbaum, F., et al. 2003, *Astronomy & Astrophysics*, 411, 123
- Groenewegen, M. A. T. 1994, *Astronomy & Astrophysics*, 290, 531
- Habing, H. J. 1996, *The Astronomy and Astrophysics Review*, 7, 97
- Habing, H. J. & Olofsson, H., eds. 2003, *Asymptotic Giant Branch Stars*, A&A Library (Springer)
- Haisch, B. M. 1979, *Astronomy & Astrophysics*, 72, 161
- Hartquist, T. & Williams, D. 1998, *The molecular astrophysics of stars and galaxies*, International series on astronomy and astrophysics (Clarendon Press)
- Herwig, F. 2005, *Annual Review of Astronomy and Astrophysics*, 43, 435
- Höfner, S. 2011, in *Astronomical Society of the Pacific Conference Series*, Vol. 445, *Why Galaxies Care about AGB Stars II: Shining Examples and Common Inhabitants*, ed. F. Kerschbaum, T. Lebzelter, & R. F. Wing, 193

- Hubeny, I. 2003, in *Astronomical Society of the Pacific Conference Series*, Vol. 288, *Stellar Atmosphere Modeling*, ed. I. Hubeny, D. Mihalas, & K. Werner, 17
- Huggins, P. J., Olofsson, H., & Johansson, L. E. B. 1988, *The Astrophysical Journal*, 332, 1009
- Justtanont, K., Skinner, C. J., Tielens, A. G. G. M., Meixner, M., & Baas, F. 1996, *The Astrophysical Journal*, 456, 337
- Justtanont, K. & Tielens, A. G. G. M. 1992, *The Astrophysical Journal*, 389, 400
- Keto, E. & Rybicki, G. 2010, *The Astrophysical Journal*, 716, 1315
- Knapp, G. R. & Morris, M. 1985, *The Astrophysical Journal*, 292, 640
- Kwok, S. 1975, *The Astrophysical Journal*, 198, 583
- Kwok, S. 2007, *Physics and chemistry of the interstellar medium* (University Science Books)
- Lombaert, R., Decin, L., de Koter, A., et al. 2013, *Astronomy & Astrophysics*, 554, A142
- Loup, C., Forveille, T., Omont, A., & Paul, J. F. 1993, *Astron. Astrophys. Suppl.*, 99, 291
- Maercker, M., Schöier, F. L., Olofsson, H., et al. 2009, *Astronomy & Astrophysics*, 494, 243
- Maercker, M., Schöier, F. L., Olofsson, H., Bergman, P., & Ramstedt, S. 2008, *Astronomy & Astrophysics*, 479, 779
- Mamon, G. A., Glassgold, A. E., & Huggins, P. J. 1988, *The Astrophysical Journal*, 328, 797
- Mihalas, D., Kunasz, P. B., & Hummer, D. G. 1975, *The Astrophysical Journal*, 202, 465
- Mohamed, K. A. 2005, *High Resolution Fourier Transform Spectroscopy of Linear Molecules* (Nova Science)
- Netzer, N. & Knapp, G. R. 1987, *The Astrophysical Journal*, 323, 734
- Ng, K.-C. 1974, *Journal of Chemical Physics*, 61, 2680
- Penzias, A. A., Wilson, R. W., & Jefferts, K. B. 1974, *Phys. Rev. Lett.*, 32, 701

- Ramstedt, S., Maercker, M., Olofsson, G., Olofsson, H., & Schöier, F. L. 2011, *Astronomy & Astrophysics*, 531, A148
- Ramstedt, S., Schöier, F. L., & Olofsson, H. 2009, *Astronomy & Astrophysics*, 499, 515
- Ramstedt, S., Schöier, F. L., Olofsson, H., & Lundgren, A. A. 2008, *Astronomy & Astrophysics*, 487, 645
- Roelfsema, P. R., Helmich, F. P., Teyssier, D., et al. 2012, *Astronomy & Astrophysics*, 537, A17
- Rybicki, G. B. & Hummer, D. G. 1991, *Astronomy & Astrophysics*, 245, 171
- Sahai, R. 1990, *The Astrophysical Journal*, 362, 652
- Schöier, F. L., Maercker, M., Justtanont, K., et al. 2011, *Astronomy & Astrophysics*, 530, A83
- Schöier, F. L. & Olofsson, H. 2001, *Astronomy & Astrophysics*, 368, 969
- Schöier, F. L., Ramstedt, S., Olofsson, H., et al. 2013, *Astronomy & Astrophysics*, 550, A78
- Schöier, F. L., Ryde, N., & Olofsson, H. 2002, *Astronomy & Astrophysics*, 391, 577
- Schöier, F. L., van der Tak, F. F. S., van Dishoeck, E. F., & Black, J. H. 2005, *Astronomy & Astrophysics*, 432, 369
- van Langevelde, H. J., van der Heiden, R., & van Schooneveld, C. 1990, *Astronomy & Astrophysics*, 239, 193
- van Zadelhoff, G.-J., Dullemond, C. P., van der Tak, F. F. S., et al. 2002, *Astronomy & Astrophysics*, 395, 373
- Vlemmings, W. H. T. & van Langevelde, H. J. 2007, *Astronomy & Astrophysics*, 472, 547
- Watson, J. K. G. 2001, *Canadian Journal of Physics*, 79, 521
- Whitelock, P. A., Feast, M. W., & van Leeuwen, F. 2008, *MNRAS*, 386, 313

Acknowledgements

I would like to thank everyone who helped me get to this stage in my career. My Masters supervisor Rachel Webster (at the University of Melbourne), who believed in me, my current PhD supervisors Kay Justtanont, who taught me to question everything, and Hans Olofsson for always providing stimulating scientific discussion. I would also like to thank Per Bergman, John Black, Matthias Maercker and Sofia Ramstedt for their help, discussions and advice along the way.

My time at Onsala would not have been the same without the friendship and support of my fellow PhD students. Thanks to Sofia, Mitra, Joachim, Eskil and Lucas, who are all in a similar boat to me. And thank-you to Francesco, Per and Fabian for helping me find my way around in a new country.

Special thanks go to Lewis, for always being supportive and for making sure I ate regularly.

And finally, thank-you to the Swedish National Space Board (SNSB) for funding my position.

Taïssa

